Engineering Structures 172 (2018) 700–711

Contents lists available at ScienceDirect

Engineering Structures

journal homepage: www.elsevier.com/locate/engstruct

Quantitative assessment of resilience for earthen structures using coupled plasticity-damage model

M.H. Motamedi*, A. Iranmanesh, R. Nazari

Henry M. Rowan College of Engineering, Rowan University, Glassboro, USA

ARTICLE INFO

Keywords:
Damages
Earthen structures
Numerical simulation
Plasticity
Structural resilience

ABSTRACT

In this work, structural resiliency is revisited as a composite term which consists of three interrelated capacities. A computational platform for quantitatively assessing the disaster-resilience of earthen structures is introduced with the use of a coupled plasticity-damage constitutive model. This numerical framework addresses the collapse resistance, damage sequences, strength residual state as well as resilience metrics. In particular, the plasticity model is furnished with combined isotropic-kinematic hardening internal variables accounting for the adaptive capacity of structural resilience. To simulate the transformative capacity at structural level, the model adopts the enhanced strain finite element method capturing the propagating fracture through the structural elements. Localized failure is detected by a bifurcation analysis. A cohesive based failure criterion is also incorporated to accurately represent the constitutive softening response in the case of progressive failure. Finally, we analyzed the factors that shape the structural resilience of earthen wall in the face of lateral loading. The performance of the structural system is examined for two conditions, namely fully intact structure and pre-damaged state.

1. Introduction

Earth-based materials have been used for millennia in construction. Some earthen structures built centuries ago are still performing satisfactorily. For instance, The Great Wall of China was built nearly 2000 years ago using local materials: rammed earth, stones, baked bricks and wood. As far as strength is concerned, it is well known that natural soil, with no reinforcement or stabilizer, may not be suited for the construction of very tall structures. Nevertheless, it has been vastly used for load-bearing structures with 1–3 stories high in Australia, Brazil, Europe, USA, India, China and many other countries Foster et al. [22], Silva et al. [50], Reddy and Kumar [41], and Zami and Lee [64]. Traditional rammed earth houses in France is a good example which were built more than 100 years ago and are still in good condition today Bui et al. [12]. Over the last decade, earth has been garnering increased attention as a revival structural material for a modern construction technique. Compared to conventional mineral building materials, earth possesses particularly positive ecological qualities such as having low carbon content, low embodied energy, highly efficient hygric-thermal behavior and inherent recyclability Schroeder [49]. Not only are these aspects driving the resurgence of the earthen buildings, but the fact that in locations with relatively cheap labor and high material costs, these structures are the most cost-effective option.

However, earthen buildings are particularly vulnerable to lateral loading induced by natural hazards such as floods and earthquakes Silva et al. [50]. The presence of cracks is a type of damage often present in these constructions, which has particular influence on the structural performance. Cracks constitute preferential paths for rainfall infiltration, directly moistening the internal structural elements, substantially reducing its mechanical properties. The presence of structural cracks in earthen walls decreases their bearing capacity and stiffness, and disrupts the overall monolithic behavior of the structure (see Fig. 1) Foster et al. [22] and Tennant et al. [56].

Numerical simulation of earthen structures, especially in the platform of the finite element (FE) method, has attracted much research interest with the advent of modern computational resources. One crucial part of an FE simulation is the selection of an appropriate constitutive material model, since earth-based materials can exhibit many complex and interacting behaviors Qi et al. [40], Tonge and Ramesh [58], Motamedi and Foster [35], Lou et al. [31], Wong and Baud [61], Xie and Shao [63,62]. At low confining pressure, localized deformation in the form of shear and/or dilation bands or fractures may occur due to the growth and coalescence of micro-cracks and pores. At high confining pressure, on the contrary, delocalized irreversible deformation may occur in the form of shear-enhanced compaction. The latter response, generally accompanied by material hardening, is the result of pore collapse, grain crushing, internal locking and other microphysical mechanisms.

* Corresponding author.
E-mail addresses: Motamedi@rowan.edu (M.H. Motamedi), Iranmanesh@rowan.edu (A. Iranmanesh), Nazari@rowan.edu (R. Nazari).

https://doi.org/10.1016/j.engstruct.2018.06.050
Received 27 November 2017; Received in revised form 4 May 2018; Accepted 13 June 2018
Available online 21 June 2018
0141-0296/

Fig. 1. Damages, in form of cracks, observed in earthen buildings due to hazard-related lateral loading.

The remainder of this paper is organized as follows: Section 2 reviews the idea of resiliency and its growing application as a metric to evaluate the performance of structural systems. Section 3 briefly demonstrates a recently modified cap plasticity model for analyzing geomaterials behavior. In Section 4 first, the kinematics of a strong discontinuity are outlined. Second, to capture the initiation of the crack and its orientation, bifurcation theory is introduced. Section 5 summarizes a mixed-mode cohesive fracture model which is suitable to represent damage evolution and softening behavior of monolithic earthen structure. In Section 6, the finite element approximation using assumed enhanced strain (AES) method is briefly discussed.

Finally in Section 7, the structural performance of an earthen wall for two case scenarios, namely being structurally intact or having some level of initial damages, when is subjected to lateral load has been examined. In addition to the metric available in the literature (including maximum capacity differentiation and residual strength ratio), the proposed multi-stage structural resiliency measure has been utilized to describe the full-range nonlinear response of the structure.

2. Resilience: from conceptual frameworks to quantitative assessment

The concept of resilience has recently been widely promoted in many fields such as urbanization, social protection, ecosystems analysis as well as structural engineering. Resilience harbors different meanings in different contexts. Some authors trace back the first ‘scientific’ application to the concept of modulus of resilience adopted in the context of 19th century warship design. This idea became progressively apparent in the 1970s, where resilience was then formally defined as “the capacity of a material to absorb energy when it is deformed elastically and then, upon unloading to have this energy recovered.” Callister and Rethwisch [13]. However, in the last decade, a more elaborate conceptualization emerged where resilience is no longer simply about resistance to change and conservation of existing structures, but instead viewed as a characteristic that includes also two other dimensions: (1) the adaptive capacity of the system components, that is leading to incremental adjustments/changes in response to increasing external impact to continue operating and (2) transformative capacity leading to transformational responses. The latter response can be regarded as a process which results from insufficient adaptive resilience. These responses are said to be transformative because they aim at altering fundamentally the systems performance such that it makes the initial system untenable. These three different types of responses can be linked (at least conceptually) to different intensities of external load or impact, as shown in Fig. 2a.

The transition from conceptual frameworks to quantitative assessment of structural resilience remains controversial due to its integrative nature. In this work, structural resiliency associated with damages induced by severe loadings is revisited as a composite term which consists of three interrelated capacities (absorptive, adaptive and transformative.) Therefore, a computational platform for quantitatively assessing the disaster-resilience of earthen structures has been developed using a coupled plasticity-damage constitutive model.

3. Three-invariant cap plasticity model

In this section, the formulation and numerical implementation of a nonassociated, three-invariant cap plasticity model are briefly described. The model comprises of a pressure-dependent shear yield surface, hardening compaction cap and newly added elliptical tension cap accounting for the tensile yielding as shown in Fig. 3. This modified model allows us to better replicate complex mechanical behaviors of earthen materials under various loading conditions. For more details and motivation of the model, the reader is referred to Motamedi and Foster [35] and the references therein.

3.1. Non-associated plastic flow rule

The generalized Hooke’s law for linear isotropic elasticity can be written as:

$$\dot{\boldsymbol{\sigma}} = \boldsymbol{C}^e : \dot{\boldsymbol{\epsilon}} \; ; \quad \boldsymbol{C}^e = \lambda \mathbf{1} \otimes \mathbf{1} + 2\mu \boldsymbol{I} \tag{3.1}$$

where $\mathbf{1}$ is the second order identity tensor, $\boldsymbol{I}$ is the fourth-order symmetric identity tensor, λ and μ are the Lamé parameters and $\boldsymbol{C}^e$ is the fourth-order isotropic elasticity tensor. The hypothesis of small deformations and rotations allows an additive decomposition of the total strain rate $\dot{\boldsymbol{\epsilon}}$ into the elastic and plastic parts:

$$\dot{\boldsymbol{\epsilon}} = \dot{\boldsymbol{\epsilon}}^e + \dot{\boldsymbol{\epsilon}}^p \tag{3.2}$$

For geomaterials, nonassociated plasticity is usually needed to realistically describe volumetric deformation Borja [8] and Collins [16]. As pointed out by McDowell [33], non-associativity in geological materials is attributed to the procedure of structural rearrangement. This physical phenomenon has been observed in conjunction with growth of microcracks, propagation of shear bands, and frictional shear resistance of geological materials. Moreover, Borja [6] demonstrates that non-associative flow rule enhances liquefaction instability in fluid-saturated granular soils. This imperative feature also allows for bifurcation (onset of strain localization) in the material from a computational standpoint Motamedi et al. [34] and Regueiro and Foster [43]. Hence, a non-associative flow rule is introduced for plastic flow as below

$$\dot{\boldsymbol{\epsilon}}^p = \dot{\gamma} \frac{\partial g(\boldsymbol{\sigma}, \boldsymbol{q})}{\partial \boldsymbol{\sigma}} \tag{3.3}$$

where g stands for a plastic potential function and $\boldsymbol{q}$ represents the stress-like plastic internal variables characterizing the hardening response of the material. $\dot{\gamma}$ is a plastic consistency parameter satisfying the Kuhn-Tucker complementary conditions Borja [8]. In addition, the continuum elasto-plastic tangent $\boldsymbol{C}^{ep}$ can be derived as the following

$$\dot{\boldsymbol{\sigma}} = \boldsymbol{C}^{ep} : \dot{\boldsymbol{\epsilon}} \; ; \quad \boldsymbol{C}^{ep} = \left(\boldsymbol{C}^e - \frac{1}{\chi} \boldsymbol{C}^e : \frac{\partial g}{\partial \boldsymbol{\sigma}} \otimes \frac{\partial f}{\partial \boldsymbol{\sigma}} : \boldsymbol{C}^e \right) \tag{3.4}$$

in which

$$\chi = \frac{\partial f}{\partial \boldsymbol{\sigma}} : \boldsymbol{C}^e : \frac{\partial g}{\partial \boldsymbol{\sigma}} - \frac{\partial f}{\partial \boldsymbol{\alpha}} : \boldsymbol{h}^{\alpha} - \frac{\partial f}{\partial \kappa} h^{\kappa} \tag{3.5}$$

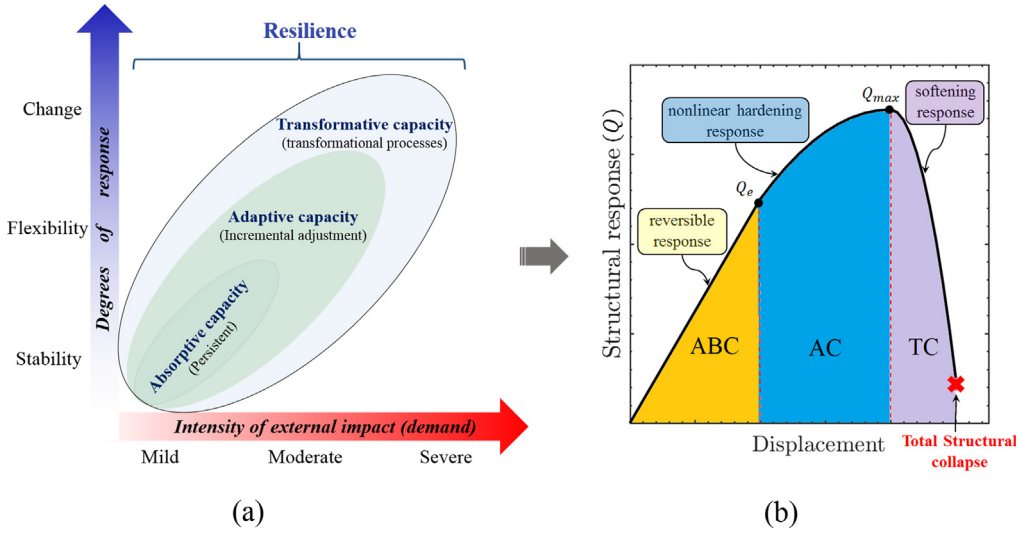

Fig. 2. Structural resilience: (a) Conceptual view as the result of absorptive (ABC), adaptive (AC), and transformative (TC) capacities, (b) proposed quantitative model: $\Omega_{Res} = E_{ABC} \cup E_{AC} \cup E_{TC}$; Q_{max} denotes maximum bearing capacity of the structure beyond which the global softening response begins; Q_e is the maximum level of the applied load for which the whole structure is still undamaged.

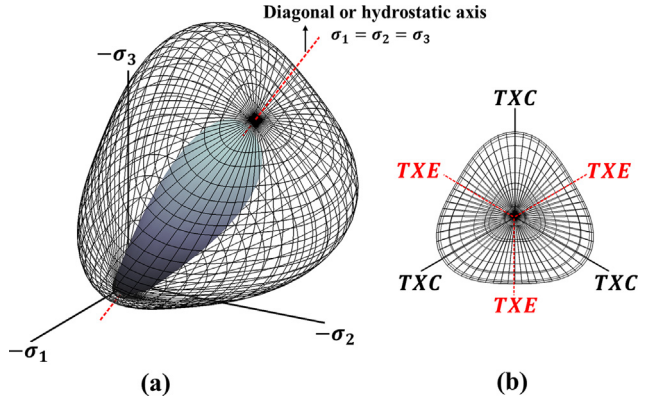

Fig. 3. Cap plasticity model: (a) three dimensional view of the yield surface (the exterior free mesh surface) and plastic potential surface (the interior gry solid) in principal stress space; (b) octahedral view, which corresponds to looking down the hydrostatic axis (lines of triaxial compression (TXC), triaxial extension (TXE) marked).

3.2. Yield surfaces

Assuming that the yielding behavior is isotropic, the yield surfaces can be expressed in terms of stress invariants (e.g. I_1, J_2 and J_3). In the case of kinematic hardening, a deviatoric backstress tensor $\boldsymbol{\alpha}$ is presented to capture the Bauschinger effect, such that the relative stress tensor can be defined as $\boldsymbol{\xi} = \boldsymbol{\sigma} - \boldsymbol{\alpha}$. Given a back stress with an appropriate translation rule, the yielding of the material may be expressed in terms of invariants of the relative stress (I_1, J_2^{ξ} and J_3^{ξ}).

Many cap plasticity models have been proposed, for example Spiezia et al. [53], Lu and Fall [32], Kohler and Hofstetter [30], Vorobiev [59], and Grueschow and Rudnicki [27]. In this work, we follow a smooth cap formulation initially proposed by Fossum and Brannon [19] and modified by Motamedi and Foster [35] thereafter. The yield function f and conjugated plastic potential g take the following form:

$$f = \Gamma(\beta^{\xi})\sqrt{J_2^{\xi}} - \sqrt{F_c}\,(F_f - N) \tag{3.6}$$

$$g = \Gamma(\beta^{\xi})\sqrt{J_2^{\xi}} - \sqrt{F_c^g}\,(F_f^g - N) \tag{3.7}$$

where the material parameter N indicates the maximum allowed translation of the initial yield surface during kinematic hardening and Γ accounts for the difference in triaxial extension vs. compression strength. The Lode angle β^{ξ} is the function of second and third invariants of the deviatoric relative stress devξ. The exponential shear failure function F_f and the corresponding plastic potential surface F_f^g are given as

$$F_f(I_1) = A - C\exp(B\,I_1) - \theta I_1 \tag{3.8}$$

$$F_f^g(I_1) = A - C\exp(L\,I_1) - \phi I_1 \tag{3.9}$$

The shear failure surface F_f captures the pressure dependence of the shear strength of the material where A, B, C and θ are all non-negative material parameters determined from peak stress experimental data, using a procedure described in Fossum and Brannon [19]. L and ϕ are determined from experimental measurements of volumetric plastic deformation. The cap function F_c generates two smooth elliptical caps to the yield function in both tensile and compressive stress zones. This function couples hydrostatic and deviatoric stress-induced deformation of the material. The cap function F_c and the corresponding one for plastic potential F_c^g are formulated as

$$F_c(I_1, \kappa) = 1 - H(\kappa - I_1)\left(\frac{I_1 - \kappa}{X(\kappa) - \kappa}\right)^2 - H(I_1 - I_1^T)\left(\frac{I_1 - I_1^T}{3T - I_1^T}\right)^2 \tag{3.10}$$

$$F_c^g(I_1, \kappa) = 1 - H(\kappa - I_1)\left(\frac{I_1 - \kappa}{X^g(\kappa) - \kappa}\right)^2 - H(I_1 - I_1^T)\left(\frac{I_1 - I_1^T}{3T^g - I_1^T}\right)^2 \tag{3.11}$$

where κ stands for the branch point in which combined porous/microcracked yield surface deviates from the nonporous profile for full dense bodies. The function $X(\kappa)$ is the intersection of the cap surface with the I_1 axis in the $\sqrt{J_2}$ versus I_1 plane and signifies the position at which pressure under pure hydrostatic loading would be sufficient to prompt grain crushing and pore collapse mechanisms (see Fig. 4).

Furthermore, this plasticity model contains two internal variables, $\boldsymbol{\alpha}$ and κ. The translational back stress tensor $\boldsymbol{\alpha}$ is adopted to capture kinematic hardening. Additionally, on the cap surface, κ is a scalar isotropic hardening parameter, which allows the yield surface to isotropically expand. The combined isotropic/kinematic hardening of the cap model is visualized by the schematic diagram in Fig. 5. The description of evolution laws for isotropic/kinematic hardening parameters and their correspondence with microstructural deformations are discussed in Motamedi and Foster [35]. It should be mentioned that, although the softening behavior is also of importance in many

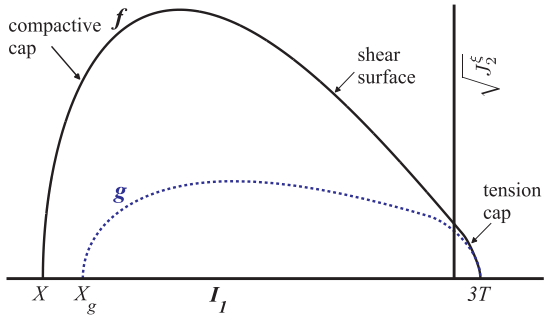

Fig. 4. Two-dimensional representation of yield (solid curve) and potential (dash curve) surfaces in meridional stress space; deviatoric stress $\sqrt{J_2}$ versus mean stress I_1.

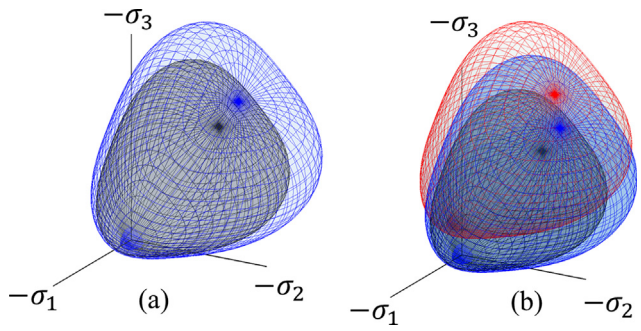

Fig. 5. Three dimensional view of initial yield surface (the interior gray solid) evolution in principal stress space for: (a) isotropic hardening (blue mesh surface) and (b) mixed isotropic-kinematic hardening (red mesh surface). (For interpretation of the references to color in this figure legend, the reader is referred to the web version of this article.)

structural engineering problems, this plasticity model is only able to capture the hardening zone of responses. Hence, as we discussed in Section 5, to represent the fracture propagation and associated softening behavior, an appropriate traction-separation model needs to be added to the current plasticity model.

3.3. Numerical implementation

Numerical integration of the constitutive models plays a key role in successfully modeling boundary value problems in engineering. Herein, a well-established integration technique called the implicit return mapping algorithm is invoked Foster et al. [20]. This algorithm affords first-order accuracy while satisfying the conditions for unconditional stability. To solve the non-linear material model, we employ the well-known Newton-Raphson (N-R) iterative method. This method basically constructs the residual vector $\boldsymbol{R}$ as a function of the unknown variables $\boldsymbol{X} = \{\boldsymbol{\sigma}, \boldsymbol{\alpha}, \kappa, \Delta\gamma\}$. The implicit stress-integration algorithm is summarized in Box 1 for a given strain increment, $\Delta\boldsymbol{\epsilon}_{n+1}$.

Box 1. Implicit stress-point algorithm for cap plasticity model.

Step 1: Compute trial state variables: $\boldsymbol{\sigma}^{tr}_{n+1} = \boldsymbol{\sigma}_n + \boldsymbol{c}^e$: $\Delta\boldsymbol{\epsilon}_{n+1}$, $\boldsymbol{\alpha}^{tr}_{n+1} = \boldsymbol{\alpha}_n$, $\kappa^{tr}_{n+1} = \kappa_n$.
Step 2: Check the yielding condition: $f^{tr}_{n+1} > 0$?
If no, set $\boldsymbol{\sigma}_{n+1} = \boldsymbol{\sigma}^{tr}_{n+1}$, $\boldsymbol{\alpha}_{n+1} = \boldsymbol{\alpha}_n$, $\kappa_{n+1} = \kappa_n$ and exit.
If yes, Go to step 3
Step 3: Apply particular mathematical treatments to reduce the number of unknowns and hence improve the computational efficiency (see Motamedi and Foster [35]):
Step 4: Initialize $\boldsymbol{X}_0 = \boldsymbol{0}$ and use N-R scheme to solve for converged solution:
$\delta\boldsymbol{X}^{(k+1)} = [D\boldsymbol{R}/D\boldsymbol{X}]^{-1}\boldsymbol{R}(\boldsymbol{X}^k)$
$\boldsymbol{X}^{(k+1)} = \boldsymbol{X}^{(k)} + \delta\boldsymbol{X}^{(k+1)}$
Until $||\boldsymbol{R}(\boldsymbol{X})||/||\boldsymbol{R}(\boldsymbol{X}_0)|| < \text{tol}_X$
where $k+1$ refers to the current iteration.
Step 5: Update state variables $\boldsymbol{\sigma}_{n+1}$, $\boldsymbol{\alpha}_{n+1}$, κ_{n+1} and consistency parameter γ_{n+1} then exit.

4. Strong discontinuity

4.1. Kinematics and governing equations

For strong discontinuities, the displacement field experiences a spatial jump $[\![\boldsymbol{u}]\!] = \boldsymbol{u}^+ - \boldsymbol{u}^-$ across the material surface Sseparating the subdomains Ω^- and Ω^+ of an otherwise continuous body Ω, see Fig. 6. The continuous displacements are distributed throughout the volume while the spatial jump vector is contained on the discontinuity surface S.

$$\boldsymbol{u}(\boldsymbol{x}, t) := \underbrace{\bar{\boldsymbol{u}}(\boldsymbol{x}, t)}_{\text{continuous part}} + \underbrace{[\![\boldsymbol{u}(t)]\!] H_S(\boldsymbol{x})}_{\text{jump discontinuity}} \tag{4.1}$$

in which $H_S(\boldsymbol{x})$ is the Heaviside function across the discontinuity surface.

In this study, it is assumed that the jump discontinuity $[\![\boldsymbol{u}]\!]$ is piecewise constant along surface S (i.e. independent of x) so that the gradient $\nabla[\![\boldsymbol{u}]\!]$ is ignored. The total strain rate tensor resulting from this

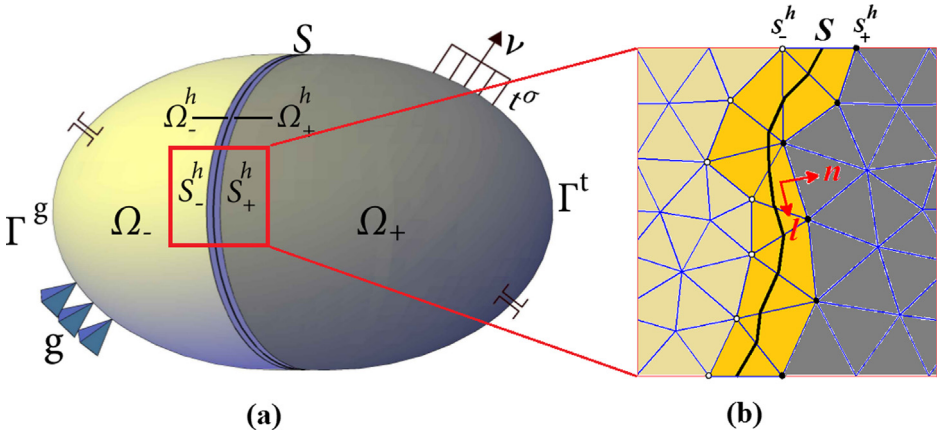

Fig. 6. (a) Body Ω with planar strong discontinuity S fixed at the reference configuration ($\Omega = \Omega^+ \cup \Omega^- \cup S$, $\Gamma = \Gamma^t \cup \Gamma^g$) (b) S^h_- and S^h_+ for a given set of localized elements; black circles indicate active nodes and white-filled circles represent inactive ones. Vectors $\boldsymbol{n}$ and l indicate the normal and tangential separations across the S^e, respectively; Superscript h corresponds to the finite element discretization of body Ω.

field is the symmetric component of the displacement gradient tensor, which can be derived in compact form as below

$$\dot{\boldsymbol{\epsilon}} := \underbrace{\operatorname{sym}(\nabla \dot{\boldsymbol{u}})}_{\text{regular part}} + \underbrace{\operatorname{sym}([\![\dot{\boldsymbol{u}}]\!] \otimes \boldsymbol{n})\delta_S}_{\text{singular part}} \tag{4.2}$$

where $\boldsymbol{n}$ is the unit normal vector to the surface S and pointing in the direction of Ω^+. The Dirac delta distribution δ_s indicates unbounded strain at the discontinuity interface.

The local form of quasi-static, isothermal equilibrium for a body with strong discontinuity leads to the following set of governing equations

$$\nabla \cdot \boldsymbol{\sigma} + \boldsymbol{b} = \boldsymbol{0} \quad \text{in } \Omega \tag{4.3a}$$

$$\boldsymbol{\sigma} \cdot \boldsymbol{\nu} = \boldsymbol{t}^{\sigma} \quad \text{on } \Gamma^t \tag{4.3b}$$

$$\boldsymbol{u} = \boldsymbol{u}_g \quad \text{on } \Gamma^g \tag{4.3c}$$

$$[\![\boldsymbol{\sigma}]\!] \cdot \boldsymbol{n} = \boldsymbol{0} \quad \text{across } S \tag{4.3d}$$

where $\boldsymbol{\sigma}$ is the Cauchy stress tensor, $\boldsymbol{b}$ the body force vector, $\boldsymbol{\nu}$ the outward unit normal vector to Γ^t, $\boldsymbol{t}^{\sigma}$ the traction on Γ^t, $\boldsymbol{u}_g$ the prescribed displacement on Γ^g, and $[\![\boldsymbol{\sigma}]\!]$ is the jump in stress across S.

4.2. Bifurcation theory: onset of localization

Given the above kinematics, it is possible to derive the conditions for localization from principles of continuum mechanics. Here, the localization condition is detected in terms of bifurcation analysis Akpama et al. [1], Chemenda and Mas [15], Motamedi et al. [34], Tjioe and Borja [57], Borja et al. [11], Regueiro and Foster [43], and Foster et al. [21]. This theory is originated in Hill [28] work which explores the onset of inelastic behavior in solids using the physics of wave propagation through the matter. In Rudnicki and Rice [46] used this work to develop a rigorous mathematical framework for detecting shear band localization. Later, Ortiz and coworkers [37] integrated this into a finite element form which has been used widely since.

To form or propagate a discontinuity, the traction must be continuous across the discontinuity surface. For continuous bifurcation, given the plasticity constitutive model proposed earlier in Section 2, the stress rate on the discontinuity surface $\dot{\boldsymbol{\sigma}}^1$ and outside that $\dot{\boldsymbol{\sigma}}^0$ can be written as below

$$\dot{\boldsymbol{\sigma}}^1 = \underbrace{\left(\boldsymbol{C}^e - \frac{1}{\chi}\boldsymbol{C}^e : \frac{\partial g}{\partial \boldsymbol{\sigma}} \otimes \frac{\partial f}{\partial \boldsymbol{\sigma}} : \boldsymbol{C}^e\right)}_{\widetilde{\boldsymbol{C}}^{ep}} : \dot{\boldsymbol{\epsilon}}^0 + \underbrace{\left(\boldsymbol{C}^{ep} - \frac{\boldsymbol{C}^e : \frac{\partial g}{\partial \boldsymbol{\sigma}} \otimes \frac{\partial f}{\partial \boldsymbol{\sigma}} : \boldsymbol{C}^e}{\frac{\partial f}{\partial \boldsymbol{\sigma}} : \boldsymbol{C}^e : \frac{\partial g}{\partial \boldsymbol{\sigma}}}\right)}_{\widetilde{\boldsymbol{C}}^{ep}} : \operatorname{sym}([\![\dot{\boldsymbol{u}}]\!] \otimes \boldsymbol{n})\delta_S \tag{4.4a}$$

$$\dot{\boldsymbol{\sigma}}^0 = \overline{\boldsymbol{C}}^{ep} : \dot{\boldsymbol{\epsilon}}^0 \tag{4.4b}$$

where $\widetilde{\boldsymbol{C}}^{ep}$ is recognized as the elastic-perfectly plastic tangent modulus.

Imposing the traction continuity requirement ($\dot{\boldsymbol{\sigma}}^1 \cdot \boldsymbol{n} = \dot{\boldsymbol{\sigma}}^0 \cdot \boldsymbol{n}$) concludes the classical condition on the localization tensor $\widetilde{\boldsymbol{A}}$ already identified in [43].

$$\underbrace{(\boldsymbol{n} \cdot \widetilde{\boldsymbol{C}}^{ep} \cdot \boldsymbol{n})}_{\widetilde{\boldsymbol{A}}} [\![\dot{\boldsymbol{u}}]\!] \delta_S = 0$$

$$\Rightarrow \det \widetilde{\boldsymbol{A}} = 0 \quad \text{for } [\![\dot{\boldsymbol{u}}]\!] \neq \underline{0} \tag{4.5}$$

in which $\boldsymbol{n}$ indicates the most critical orientation of the discontinuity surface in the localized element. The above equation states that a nontrivial solution for the traction continuity condition is, of course, possible only when $\widetilde{\boldsymbol{A}}$ is singular.

Following Foster et al. [21], we use a numerical algorithm to solve $\det \widetilde{\boldsymbol{A}} = 0$ for the band normal $\boldsymbol{n}$ and then $\widetilde{\boldsymbol{A}}[\![\dot{\boldsymbol{u}}]\!] = \boldsymbol{0}$ for the deformation directions at the inception of localization. Note that the algorithm is modified somewhat from the original form, as plasticity models for geomaterials often have non-associative or kinematically hardening components. These features destroy the major symmetry of the tangent modulus. Fortunately, the patch is relatively simple and can be accomplished simply by symmetrizing the matrix referred to as $\boldsymbol{J}$ in Ortiz et al. [37].

5. Softening response

5.1. Traction-separation model

In this section, a post-localization model is introduced to describe the softening response of the material after localization detection. In particular, a novel cohesive traction-separation law recently presented in Weed et al. [60] is utilized to characterize the macro-crack evolution in terms of the displacement jump on the slip surface S. Therefore, similar to the concept of cohesive zone models for quasi-brittle materials (see Parvaneh and Foster [39], Remmers et al. [44], de Borst et al. [17], Sancho et al. [47], Camacho and Ortiz [14], among others), a damage-like function F is proposed in two forms of the tensile and compressive regime, (5.1a) and (5.1b). Schematic Fig. 7 demonstrates how the elliptical damage surface $F = 0$ shrinks to the origin while c_{eq} decreases linearly toward zero as the equivalent displacement jump increases. In addition, for the compressive case (i.e., crack closure), the frictional resistance always operates on the crack surface independently of the softening process. Once the cohesion strength completely degrades ($\zeta_{max} = \zeta_c$), the cohesive crack surface evolves to a Coulomb friction surface with friction coefficient $\mu = \tan\phi'$.

$$F_{\text{tension}} = \underbrace{\sqrt{(\tau_s)^2 + (\alpha_\sigma \sigma_n)^2}}_{\sigma_{\text{eq}}} - c_{\text{eq}} \tag{5.1a}$$

$$F_{\text{compression}} = |\tau_s - c_{\text{eq}} \cdot \operatorname{sign}(\zeta_s)| - \mu - \sigma_n \tag{5.1b}$$

where the normal traction $\sigma_n = \boldsymbol{n} \otimes \boldsymbol{n} : \boldsymbol{\sigma}$ and tangential traction $\tau_s = \boldsymbol{n} \otimes \boldsymbol{l} : \boldsymbol{\sigma}$ attribute to the slip surface. The notation • represents the

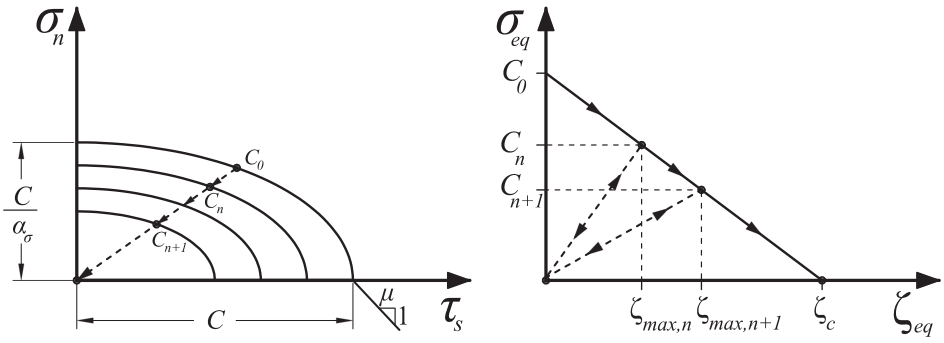

Fig. 7. Cohesive fracture law: (a) isotropic softening of the damage-like surface $F = 0$ in traction (σ_n, τ_s) space (b) equivalent traction-separation relationship with corresponding loading-unloading paths. ζ_{max} indicates the maximum attained equivalent separation.

Macaulay brackets, taking into account the positive portion, α_σ is a normal stress weighting factor and $\mu = \tan\phi'$ is a static coefficient of friction on the slip surface. Moreover, the non-negative parameters σ_{eq} and c_{eq} indicate the equivalent traction and equivalent cohesive strength of the band, respectively. Notably, the term sign(ζ_s) devised in Eq. (5.1b) would imply that the cohesion on the slip surface operates as a restoring force, i.e. the force c_{eq} always acts in the opposite direction of the displacement jump (or separation) vector. Note that the initial cohesion c_0 must be computed in a manner to be balanced with the bulk stress state at the moment of localization. In other words, initial cohesion is assumed as a non-constant parameter whose value depends on a loading history of the material before localization. For our particular formulation, the damage model follows the spirit of localized damage mechanics, so that the crack surface softens with the increase of displacement, but unloads/reloads elastically.

In previous studies, various cohesion softening laws have been proposed for a wide range of materials, such as trapezoidal function for a high-strength-low-alloy (HSLA) steel [48]; exponential function for a steel [38]; linear softening function for a polycrystalline brittle materials [18,4]; and linear, bilinear, and exponential softening functions for concrete [24,3]. In this work, as shown in Eq. (5.2), a linear softening curve is utilized given that for earthen materials, it has been shown a linear softening model fits experimental data well [45,29].

$$c_{eq} = c_0\left(1-\frac{\zeta_{max}}{\zeta_c}\right) \tag{5.2}$$

where ζ_c denotes to the characteristic slip (or separation) distance, beyond which complete failure occurs in the sense that the crack surface entirely loses its cohesive strength. The scalar ζ_{eq} indicates the equivalent jump magnitude and takes the form of

$$\zeta_{eq} = \sqrt{\zeta_s^2 + (\alpha_\zeta \zeta_n)^2} \tag{5.3}$$

in which the variables ζ_n and ζ_s are normal opening and tangential (in-plane sliding) slip on the localization band. The parameter α_ζ is a coefficient weighing the relative contribution of the opening and sliding modes in the damage process. Following the spirit of damage mechanics in the unloading/reloading case, we assume c_{eq} unloads elastically to the origin. Likewise, the reloading path is also considered elastic until the point of maximum equivalent separation ζ_{max} attained up until the current time. Beyond this point the softening process will resume. The slope of the unloading-reloading curve can be thought of as the stiffness of the cohesion force and derived as

$$k_c = \frac{c}{\zeta_{max}} = c_0\left(\frac{1}{\zeta_{max}}-\frac{1}{\zeta_c}\right) \tag{5.4}$$

Subsequently, the equivalent stress on the band can be rewritten as

$$\sigma_{eq} = k_c \zeta_{eq} \tag{5.5}$$

5.2. Model's relationship to fracture energy

The specific fracture energy G is the amount of external energy required to form a unit surface area of the fully-separated (or damaged) crack. This softening property can be simply computed from the area under the traction-separation function in Fig. 7b. In view of this fact, we can assign different specific fracture energies to each of the respective failure modes (I and II) by assigning $\alpha_\sigma, \alpha_\zeta \neq 1$.

$$\alpha_\sigma \alpha_\zeta = \frac{G_{II}}{G_I} \tag{5.6}$$

In this work, we will assume $\alpha_\sigma = \alpha_\zeta$, hence

$$\alpha_\sigma = \alpha_\zeta = \left(\frac{G_{II}}{G_I}\right)^{\frac{1}{2}} \tag{5.7}$$

5.3. Numerical implementation

As discussed in detail by [36], if material failure propagates through the solids, the tangent constitutive operator $\boldsymbol{C}^{alg}_{n+1}$ progressively loses its positive definite character which is eventually accompanied by the loss of positive definiteness of the global stiffness matrix. Hence, we adopt the implicit/explicit (Impl-Ex) integration technique to solve the slip values. Strictly speaking, seeking solution at time step t_{n+1} for a given localized element, the displacement jump (slip values) $\boldsymbol{\zeta} = (\zeta_n, \zeta_s)$ are explicitly approximated based on their implicitly updated values from prior time steps t_n and t_{n-1}.

$$\widetilde{\boldsymbol{\zeta}}_{n+1} = \boldsymbol{\zeta}_n + \frac{\Delta t_{n+1}}{\Delta t_n}(\boldsymbol{\zeta}_n - \boldsymbol{\zeta}_{n-1}) \tag{5.8}$$

The semi-implicit stress is then calculated

$$\widetilde{\boldsymbol{\sigma}}_{n+1} = \boldsymbol{\sigma}_n + \boldsymbol{c}^e : \Delta\boldsymbol{\varepsilon}^{conf}_{n+1} - \boldsymbol{c}^e : (\widetilde{\boldsymbol{\zeta}}_{n+1} \otimes \nabla f^h)^s \tag{5.9}$$

since $\widetilde{\boldsymbol{\zeta}}_{n+1}$ is postulated as a predetermined vector, we can easily derive the effective algorithmic operator C^{eff}_{n+1} as below

$$\boldsymbol{C}^{eff}_{n+1} = \frac{\partial \widetilde{\boldsymbol{\sigma}}_{n+1}}{\partial \boldsymbol{\varepsilon}_{n+1}} = \boldsymbol{C}^e \tag{5.10}$$

As can be seen above, for linear elasticity, the tangent modulus is constant. This approach, at minor cost of accuracy, improved the efficiency of the simulation by creating a linear solution in this part. In the end, once the convergent solution of the global displacements is assured, the internal variables can be updated implicitly at time step t_{n+1} using Newton-Raphson method:

$$\boldsymbol{\zeta}^{k+1}_{n+1} = \boldsymbol{\zeta}^k_{n+1} - \left(\frac{\partial \boldsymbol{r}^e_{enh}(\boldsymbol{\zeta}^k_{n+1})}{\partial \boldsymbol{\zeta}^k_{n+1}}\right)^{-1} \boldsymbol{r}^e_{enh}(\boldsymbol{\zeta}^k_{n+1}) \tag{5.11}$$

where $k+1$ refers to the current iteration. Recall Eq. (5.1), the local residual vector $\boldsymbol{r}^e_{enh} = \begin{Bmatrix}\Phi_1\\ \Phi_2\end{Bmatrix}$ can be defined based on traction balances on the discontinuity surface as below

$$\Phi_1 = \sigma_n - k_c\zeta_n = 0 \tag{5.12a}$$

$$\Phi_2 = |\tau_s - k_c\zeta_s| - \mu - \sigma_n = 0 \tag{5.12b}$$

To avoid repetition, the explicit representations of derivatives are not derived here. We refer to Weed et al. [60] for complete details.

6. Finite element implementation

6.1. Enhanced finite element formulation

In order to incorporate strong discontinuity analysis into the platform of finite element simulation, the assumed enhanced strain (AES) method based on the Hu-Washizu principle is invoked [6,21,51]. Fig. 8 demonstrates the underlying idea behind the enhanced finite element implementation for a constant strain triangle (CST) element. In this approach, the displacement discontinuity is conceptualized as an appropriate incompatible mode and added to the standard FE solutions. It is worth noting that the AES method is numerically appealing technique since the enhancements for discontinuities are condensed out locally and hence no additional global degrees of freedom are added to the calculations. The standard static condensation algorithm is considered accordingly to confine the enhancement within the element level.

The strain rate tensor for infinitesimal deformation is written as

$$\dot{\boldsymbol{\epsilon}} = \nabla^s \dot{\boldsymbol{u}} = \underbrace{\nabla^s \dot{\tilde{\boldsymbol{u}}}}_{conforming} + \underbrace{(-[\![\dot{\boldsymbol{u}}]\!] \otimes \nabla f^h)^s + ([\![\dot{\boldsymbol{u}}]\!] \otimes \boldsymbol{n})^s \delta_S}_{enhanced} \tag{6.1}$$

which can be regularized in a form of

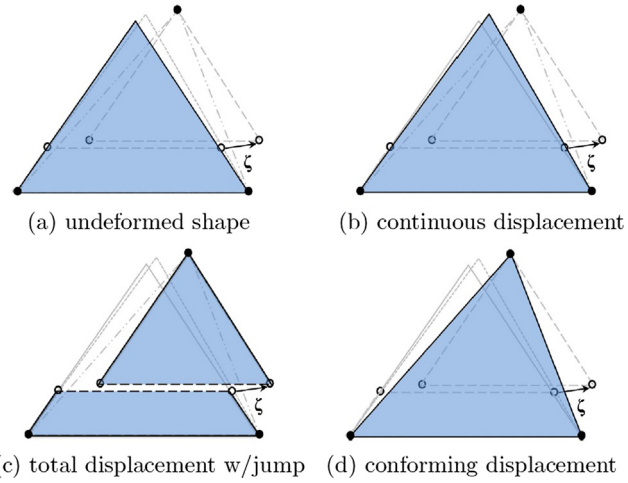

Fig. 8. Enhancing a CST finite element: (a) corresponds to an undeformed element, in (b) the element has undergone an arbitrary displacement $\bar{u}(x, t)$ and (c) is the total displacement after experiencing a displacement jump $[\![u(t)]\!]$ and finally (d) is the conforming displacement of the element $\tilde{u}(x, t)$.

Table 1
Material parameters for Salem limestone rock adopted in this simulation.

Parameter	Value
Young's modulus (E)	22,547 (MPa)
Poisson's ratio (ν)	0.2524 (dimensionless)
Compression cap parameter (κ_0)	−8.05 (MPa)
Shear yield surface parameter (A)	689.2 (MPa)
Shear yield surface parameter (B)	3.94e−4 (1/MPa)
Shear yield surface parameter (L)	1.0e−4 (1/MPa)
Shear yield surface parameter (C)	675.2 (MPa)
Shear yield surface parameter (θ, ϕ)	0.0 (rad)
Aspect ratios (R, Q)	28.0 (dimensionless)
Tension cap parameter (I_1^T)	0.0 (MPa)
Isotropic tensile strength (T)	5 (MPa)
Isotropic tensile strength (T^g)	10 (MPa)
Isotropic hardening parameter (W)	0.08 (dimensionless)
Isotropic hardening parameter (D_1)	1.47e−3 (1/MPa)
Isotropic hardening parameter (D_2)	0.0 (1/MPa^2)
Kinematic hardening parameter (c^α)	1e5 (MPa)
Kinematic hardening parameter (N)	6.0 (MPa)
Stress triaxiality parameter (ψ)	0.8 (dimensionless)
Localized friction angle (ϕ')	30° (degree)
Characteristic slip distance (ζ_c)	0.4* (mm)
Specific fracture energy ratio (G_{II}/G_I)	4.8** (dimensionless)

* An experimental value calculated for a limestone rock tested under cracked Brazilian disc configuration Al-Shayea [2]. ** An empirical value given in Borja and Foster [9].

$$\dot{\epsilon} = \nabla^s \dot{u} = \underbrace{\nabla^s \dot{\tilde{u}} + (-[\![\dot{u}]\!] \otimes \nabla f^h)^s}_{\dot{\epsilon}^{reg}} + \underbrace{([\![\dot{u}]\!] \otimes n)^s \delta_S}_{singular} \tag{6.2}$$

The function $f^h(x)$ is a smooth blending function for localized elements that can be conveniently defined as the sum of the shape functions attributed to the active nodes.

$$f^h = \sum_{A=1}^{n_{en}} N_A H_S(x_A) \tag{6.3}$$

where n_{en} is the number of nodes for a localized element, and N_A are the standard finite element shape functions. Using such a kinematic description affords the formulation the ability to allow the essential boundary conditions, Γ^g in Fig. 6, to be applied exclusively on the conforming displacement term $\tilde{u}(x, t)$. As a result, the nodal displacements calculated at the global level can be realized as the final

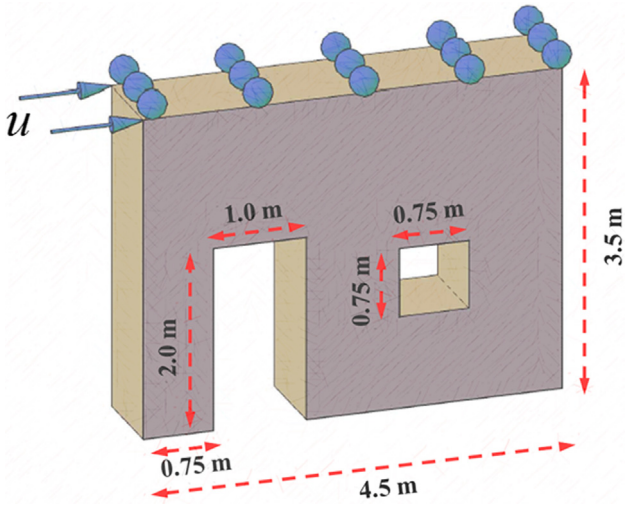

Fig. 9. Geometry and boundary conditions of an earthen wall subjected to in-plane lateral (shear) loading. Spheres stand for roller supports. As a consequence, the boundary nodes on the top edge will tend to translate only along the surface upon which the roller rests.

displacements. Eventually, the finite element stress for localized elements can be obtained from the regular part of the strain $\dot{\epsilon}^{reg}$. The relevant mathematical background is discussed in [10]. Thus, for elastic unloading we have

$$\dot{\sigma} = C^e : \dot{\epsilon}^{reg} \tag{6.4}$$

For further details of the AES method, including its variational and matrix formulation, the reader is referred to Borja [7] and the references therein.

6.2. Stiffness matrix

For the strong discontinuity approach, the resulting stiffness matrix from this formulation, assuming elastic unloading in the bulk material can be derived. We begin with two sets of equations that must be solved: the standard balance of linear momentum (here taken to be quasi-static and small strain) and the traction continuity across the discontinuity surface. In the weak form, they become Regueiro and Borja [42] and Foster et al. [21]

$$R^e = \int_{\Omega^e} B^t : \sigma \mathrm{d}\Omega - \int_{\Omega^e} N^t b \mathrm{d}\Omega - \int_{\Gamma^e} N^t t \mathrm{d}\Gamma = 0 \tag{6.5}$$

$$r^e_{enh} = 0 \tag{6.6}$$

Taking variations on these, we arrive at

$$\delta R^e = K^e_{dd} \delta d^e + K^e_{d\zeta} \delta \zeta^e \tag{6.7}$$

$$\delta r^e_{enh} = K^e_{\zeta d} \delta d^e + K^e_{\zeta\zeta} \delta \zeta^e \tag{6.8}$$

where K^e_{dd} is the standard element stiffness matrix, and the others can be shown to have the following forms:

$$K^e_{d\zeta} = -\int_{\Omega^e} B^t : c^e : \frac{\partial \epsilon}{\partial \zeta} \mathrm{d}\Omega \tag{6.9}$$

$$K^e_{\zeta d} = \frac{\partial r^e_{enh}}{\partial d^e} = \frac{\partial r^e_{enh}}{\partial \sigma} : C^e : B^e \tag{6.10}$$

$$K^e_{\zeta\zeta} = \frac{\partial r^e_{enh}}{\partial \zeta^e} = [\partial r^e_{enh}/\partial \zeta^e_n \quad \partial r^e_{enh}/\partial \zeta^e_s]^T \tag{6.11}$$

The tensor B is the third-order, symmetric gradient of the nodal displacement interpolation functions, commonly referred to as the strain-displacement tensor, i.e. $B_{ijk} d_k = \epsilon_{ij}$. The last equation is convenient

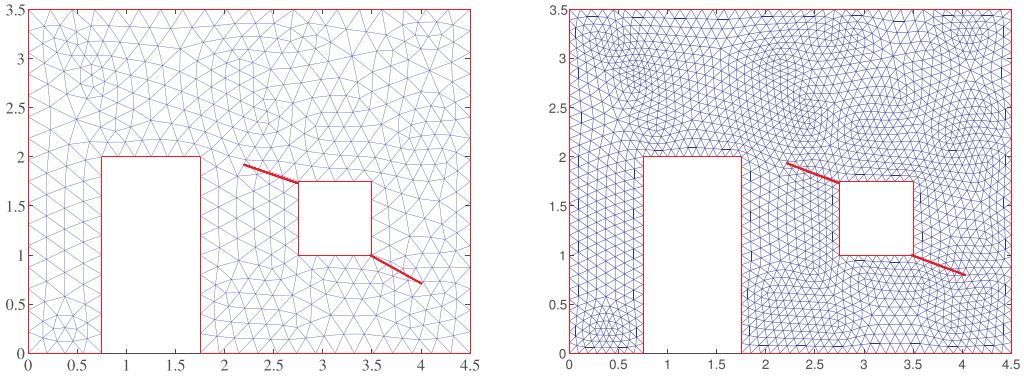

(a) Coarse mesh consists of 516 elements (b) Fine mesh consists of 1952 elements

Fig. 10. Spatial discretization of a wall of an earthen structure. In the case of pre-existing damage condition, initial cracks (marked by the red lines) are inserted into the finite element model. (For interpretation of the references to color in this figure legend, the reader is referred to the web version of this article.)

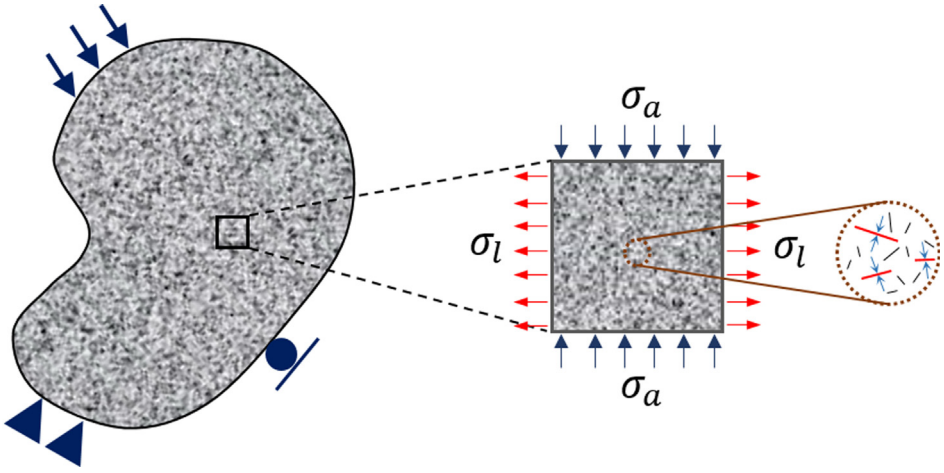

Fig. 11. Schematic representation of the localized cracked zone in the material under triaxial loading condition. The sample is subjected to a compressive axial loading ($\sigma_a < 0$). Inset shows numerous microcracks including the ones (marked by red color) whose faces are under pressure, and hence grow in a frictional sliding mode. Growth mechanism of microcracking is modeled via deviatoric Back-stress tensor $\boldsymbol{\alpha}$ ($\alpha_{ii} = 0$). (For interpretation of the references to color in this figure legend, the reader is referred to the web version of this article.)

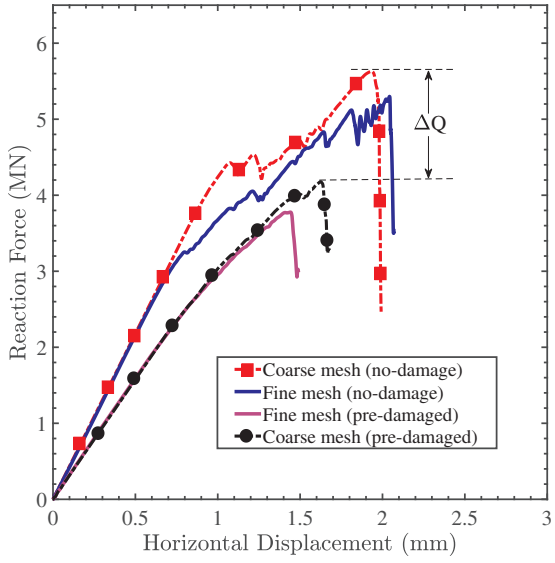

Fig. 12. Structural response to the lateral loading: Force-displacement curve of wall, with and without pre-existing damages and for different mesh sizes.

Table 2
Structural performance measurement.

Criterion	Mesh 1	Mesh 2
Residual strength ratio (dimensionless)	0.741	0.718
Robustness ΔQ (MN)	1.455	1.481
Intact structural Wall		
Absorptive capacity *ABC* (KJ)	1.42	1.18
Adaptive capacity *AC* (KJ)	5.16	5.46
Transformative capacity *TC* (KJ)	0.19	0.13
Structural Wall with pre-existing damage		
Absorptive capacity *ABC* (KJ)	1.04	1.04
Adaptive capacity *AC* (KJ)	2.49	1.73
Transformative capacity *TC* (KJ)	0.148	0.17

because it is identical to the tangent stiffness used in the local N-R for determining the slip, and the same code can be reused. Finally, the local degrees of freedom which correspond to the deformation band may be condensed out at the element level in the standard way, resulting in the final element stiffness matrix.

$$K_*^e = K_{dd}^e - K_{d\zeta}^e K_{\zeta\zeta}^{e\,-1} K_{\zeta d}^e \tag{6.12}$$

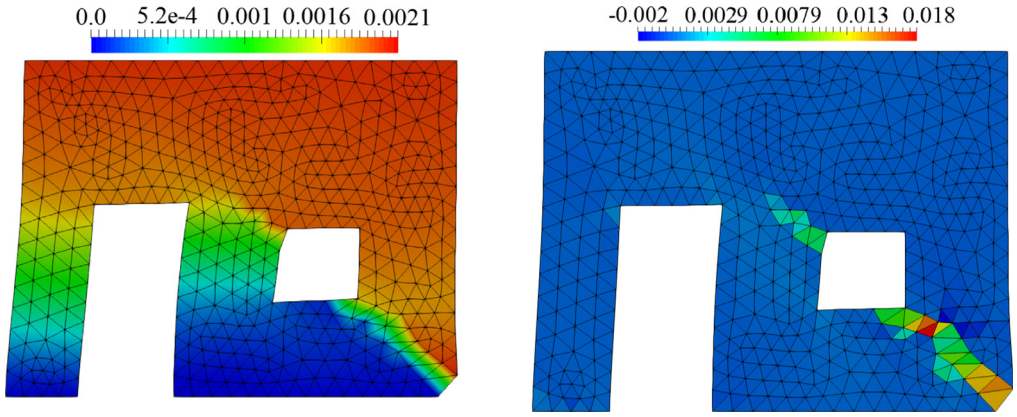

(a) Horizontal displacement contour, $dx(m)$ (b) Shear strain contour (ϵ_{12})

Fig. 13. Deformed mesh with enhanced solution of an intact wall using the mesh 1.

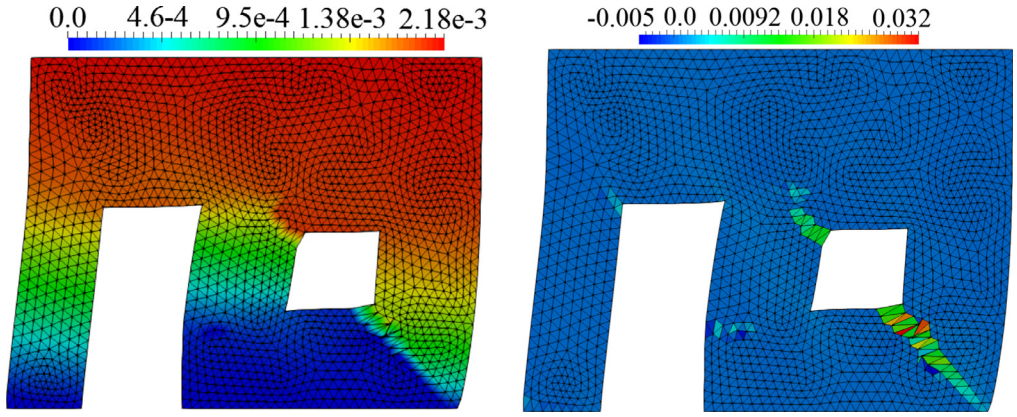

(a) Horizontal displacement contour, $dx(m)$ (b) Shear strain contour (ϵ_{12})

Fig. 14. Deformed mesh with enhanced solution of an intact wall using the mesh 2.

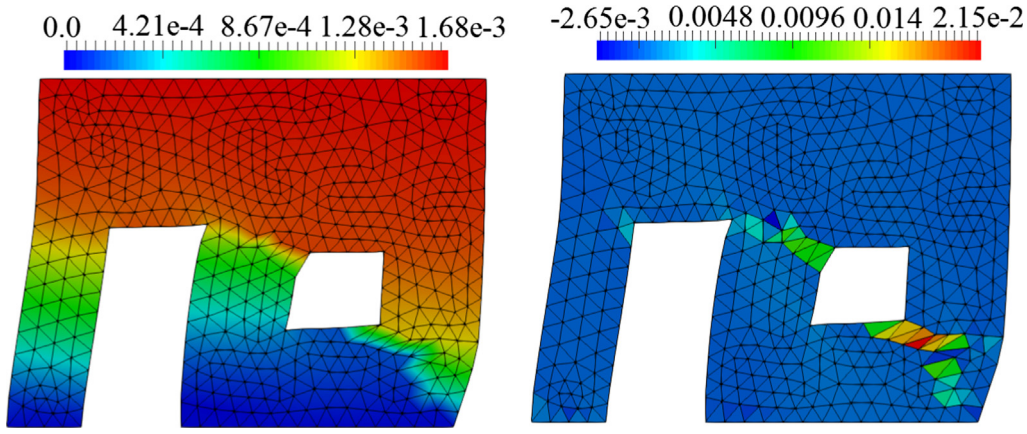

(a) Horizontal displacement contour, $dx(m)$ (b) Shear strain contour (ϵ_{12})

Fig. 15. Deformed mesh with enhanced solution of a wall with pre-existing damage shown in Fig. 10a using the mesh 1.

Considering K^e_{dd} as the standard stiffness matrix for a non-localized element, Eq. (6.12) reveals how the material stiffness degrades for a localized (i.e. damaged) element via a softening component $K^e_{d\zeta} K^e_{\zeta\zeta}{}^{-1} K^e_{\zeta d}$ reflecting primarily the development of jump displacement across the discontinuity surface S.

7. Numerical example

In this study, the material properties listed in Table 1 were fit to Salem limestone rock by Fossum and Brannon [19] and frequently reported in Regueiro and Foster [43], Sun et al. [55] and Motamedi and Foster [35]. For the specific fracture energy ratio G_{II}/G_I, varied values

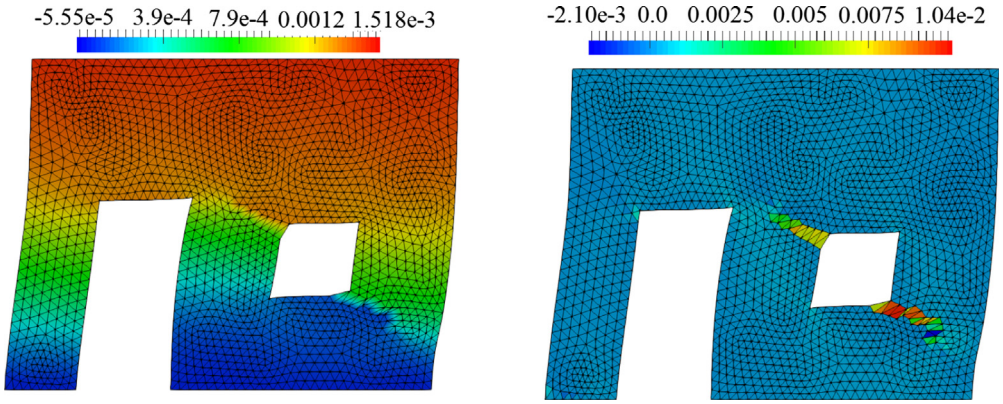

(a) Horizontal displacement contour, $dx(m)$ (b) Shear strain contour (ϵ_{12})

Fig. 16. Deformed mesh with enhanced solution of a wall with pre-existing damage shown in Fig. 10b using the mesh 2.

are calculated experimentally dependent on the specific material of the interest and the fracture test chosen. In this paper, we use the empirical value of $G_{II}/G_I = 4.8$ taken from Al-Shayea [2] for a Saudi Arabian limestone rock tested under the ambient condition using CBD configuration. For the characteristic slip distance ζ_c, the value 0.4 (mm) is assumed [9].

As an example, the shear behavior of an earthen wall for two case scenarios has been investigated. The first scenario is labeled originally intact condition presuming that the wall was not previously subjected to any damaging load or event using a nonlinear pushover or pushdown analysis. In the second one, the wall has sustained some level of damage or the brittle failure in the beginning. The geometry and boundary conditions of the problem are depicted in Fig. 9. The wall has openings for a door and a window. As shown by arrows, a shear displacement, representing a strong hazard-related force, is applied from the left. To analyze the problem under plane strain condition, two mesh sizes with 516 and 1952 CST elements have been chosen, Fig. 10. For the case of pre-damaged condition, the initial cracks are introduced in the FE model as a fully damaged part of the structure using the specific embedded discontinuity surfaces inside the elements as graphically shown in the figure by red-colored solid lines. This interface includes zero initial cohesive strength so that the pre-cracked elements immediately fail when loaded in tension, shear or any of their combinations. These elements can, however, still sustain compressive loads.

In the simulation, we assume that the material obeys the non-associative plastic flow rule, which its parameters are given in Box 2 and set stress triaxiality parameter $\psi = 0.8$ to trigger Strength Differential (SD) effect of the model (J_3^{ζ} dependence). This feature is very common of geological materials and allows the bulk to withstand more loads when its most critical surface undergoes higher compression. This behavior has been seen mainly because of pressure-induced friction acting on faces of flaws, microcracks and grain boundaries embodied with in the geomaterials, see Fig. 11.

The force-displacement curve is plotted in Fig. 12 which shows the pre-damaged condition comparing to the originally intact case, there is only a modest amount of plasticity before a brittle drop in strength and it can be quantitatively measured based on adaptive capacity. Moreover, for both cases, the residual strength remains at the end of load-carrying capacity curve (i.e. structural softening response). This is most likely due to friction effects on the discontinuity surface which indeed represents the frictional locking phenomenon once the crack closure becomes more pronounced. As for quantitative evaluation of structural robustness, the residual strength ratio $RSR = Q_{max}^{damage}/Q_{max}^{intact}$ can be defined according to Ghosn [25]. Sorensen and Christensen [52] presented the value of $RSR = 0.8$ as an acceptable structural safety limit based on the probability and consequences of failure. In addition, Bontempi et al. [5] performed a conceptual comparison between the performance of an originally intact system and that of the system with a pre-existing damage using the difference between maximum load-carrying capacities $\Delta Q = Q_{max}^{intact} - Q_{max}^{damage}$ rather than ratios. This metric has been adopted as a measure of robustness by other researchers such as Frangopol and Curley [23], Starossek and Haberland [54,26] and Giuliani [26]. Furthermore, the proposed structural resilience for different stages (i.e. absorptive, adaptive and transformative phases) can be calculated by integrating the load-carrying capacity curve over the displacement for each corresponding response, namely reversible (elastic), nonlinear hardening and softening, respectively. The computed values of aforementioned criteria are listed in Table 2. As is evident from Table 2, the major difference between the performance of intact and pre-damaged structures is related to their adaptive capacities. The existence of initial cracks not only reduces the maximum load-carrying capacity but also leads to about 50% loss of the adaptive capacity of the system. In other words, the predamaged earthen wall in part loses its original ductility performance.

Additional insights can be gained by comparing the kinematics of deformation. Accordingly, the deformed meshes generated by the AES solution are displayed in Figs. 13–16. The plot indicates that once the intact structure is laterally loaded enough, the fracture initiates from the corners of the window. Subsequently, the crack growth continues diagonally through the structure. In the pre-damaged condition, however, the cracks initiated and continued to propagate from the ends of the initially inserted discontinuity surfaces. For both cases, the track of shear bands can be clearly observed in shear strain contours depicted in Figs. 13b–16b.

8. Conclusion

The proposed numerical framework in this study successfully addresses the structural performance indicators including maximum collapse resistance, damage sequences, structural robustness, and structural resilience of monolithic earthen buildings. For the nonlinear finite element simulation, localized damage is detected by a loss of ellipticity condition, and subsequent crack growth is modeled in the framework of an enhanced strain finite element schema. In particular, a mixed isotropic-kinematic hardening plasticity model was utilized to account for the adaptive capacity of structural resilience. According to the shear resistance response, the existence of pre-damages in the system profoundly reduces the global ductility of the structure and results in more brittle structural behavior. In addition to an evident reduction in maximum load carrying capacity of the system, it has been found that the major difference between the resilience performance of intact and initially damaged structures is related to their adaptive capacities.

Acknowledgments

This work was supported through New Jersey Department of Community Affairs (NJDCA) from Superstorm Sandy Community Development Block Grant Disaster Recovery (CDBG-DR). The authors would like to acknowledge the support of NJDCA.

References

[1] Akpama H, Bettaieb MB, Abed-Meraim F. Localized necking predictions based on rate-independent self-consistent polycrystal plasticity: bifurcation analysis versus imperfection approach. Int J Plast 2017;91:205–37 <http://www.sciencedirect.com/science/article/pii/S0749641917300566>.
[2] Al-Shayea NA. Crack propagation trajectories for rocks under mixed mode iii fracture. Eng Geol 2005;81(1):84–97 <http://www.sciencedirect.com/science/article/pii/S0013795205001614>.
[3] Bazant ZP. Concrete fracture models: testing and practice. Eng Fract Mech 2002;69(2):165–205 <http://www.sciencedirect.com/science/article/pii/S0013794401000844>.
[4] Benedetti I, Aliabadi M. A three-dimensional cohesive-frictional grain-boundary micromechanical model for intergranular degradation and failure in polycrystalline materials. Comput Methods Appl Mech Eng 2013;265(0):36–62 <http://www.sciencedirect.com/science/article/pii/S0045782513001503>.
[5] Bontempi F, Gkoumas K, Arangio S. Systemic approach for the maintenance of complex structural systems. Struct Infrastruct Eng 2008;4(2):77–94.
[6] Borja RI. Condition for liquefaction instability in fluid-saturated granular soils. Acta Geotech 2006;1(4):211. http://dx.doi.org/10.1007/s11440-006-0017-5.
[7] Borja RI. Assumed enhanced strain and the extended finite element methods: a unification of concepts. Comput Methods Appl Mech Eng 2008;197(3340):2789–803 <http://www.sciencedirect.com/science/article/pii/S0045782508000315>.
[8] Borja RI. Plasticity: modeling and computation. Springer; 2013.
[9] Borja RI, Foster CD. Continuum mathematical modeling of slip weakening in geological systems. J Geophys Res: Solid Earth 2007;112(B4):1–12. http://dx.doi.org/10.1029/2005JB004056.
[10] Borja RI, Regueiro RA. Strain localization in frictional materials exhibiting displacement jumps. Comput Methods Appl Mech Eng 2001;190(2021):2555–80 <http://www.sciencedirect.com/science/article/pii/S004578250000253X>.
[11] Borja RI, Song X, Rechenmacher AL, Abedi S, Wu W. Shear band in sand with spatially varying density. J Mech Phys Solids 2013;61(1):219–34 <http://www.sciencedirect.com/science/article/pii/S0022509612001524>.
[12] Bui Q, Morel J, Reddy BV, Ghayad W. Durability of rammed earth walls exposed for 20 years to natural weathering. Build Environ 2009;44(5):912–9 <http://www.sciencedirect.com/science/article/pii/S036013230800156X>.
[13] Callister Jr. WD, Rethwisch DG. Fundamentals of materials science and engineering: an integrated approach. 4th ed. John Wiley & Sons, Ltd.; 2012.
[14] Camacho G, Ortiz M. Computational modelling of impact damage in brittle materials. Int J Solids Struct 1996;33(2022):2899–938 <http://www.sciencedirect.com/science/article/pii/0020768395002553>.
[15] Chemenda AI, Mas D. Dependence of rock properties on the lode angle: experimental data, constitutive model, and bifurcation analysis. J Mech Phys Solids 2016;96:477–96 <http://www.sciencedirect.com/science/article/pii/S0022509616302575>.
[16] Collins I. Associated and non-associated aspects of the constitutive laws for coupled elastic/plastic materials. Int J Geomech 2002;2(2):259–67.
[17] de Borst R, Remmers JJ, Needleman A. Mesh-independent discrete numerical representations of cohesive-zone models. Eng Fract Mech 2006;73(2):160–77. [advanced Fracture Mechaninc for Life Safety Assessments]. <http://www.sciencedirect.com/science/article/pii/S0013794405001852>.
[18] Espinosa HD, Zavattieri PD. A grain level model for the study of failure initiation and evolution in polycrystalline brittle materials. Part I: Theory and numerical implementation. Mech Mater 2003;35(36):333–64 <http://www.sciencedirect.com/science/article/pii/S0167663602002855>.
[19] Fossum AF, Brannon RM. The Sandia GeoModel: theory and user's guide. SAND report August. Sandia National Laboratories; 2004.
[20] Foster C, Regueiro R, Fossum A, Borja R. Implicit numerical integration of a three-invariant, isotropic/kinematic hardening cap plasticity model for geomaterials. Comput Methods Appl Mech Eng 2005;194(50–52):5109–38 <http://linkinghub.elsevier.com/retrieve/pii/S0045782505000022>.
[21] Foster CD, Borja RI, Regueiro RA. Embedded strong discontinuity finite elements for fractured geomaterials with variable friction. Int J Numer Meth Eng 2007;72(5):549–81 <http://doi.wiley.com/10.1002/nme.2020>.
[22] Foster CD, Weed DA, Motamedi MH, Tennant AG. Mechanical behavior of earthen materials in structural applications. ASCE; 2016. < http://ascelibrary.org/doi/abs/10.1061/9780784480151.068 > .
[23] Frangopol D, Curley J. Effects of damage and redundancy on structural reliability. J Struct Eng 1987;113(7):1533–49.
[24] Galvez J, Cervenka J, Cendon D, Saouma V. A discrete crack approach to normal/shear cracking of concrete. Cem Concr Res 2002;32(10):1567–85 <http://www.sciencedirect.com/science/article/pii/S0008884602008256>.
[25] Ghosn M. Performance indicators for structural systems and infrastructure networks. J Struct Eng 2016;142(9). [e. a.].
[26] Giuliani L. Structural safety in case of extreme actions. Int J Life Cycle Perform Eng 2012;1(1):22.
[27] Grueschow E, Rudnicki JW. Elliptic yield cap constitutive modeling for high porosity sandstone. Int J Solids Struct 2005;42(16–17):4574–87 <http://linkinghub.elsevier.com/retrieve/pii/S0020768305000533>.
[28] Hill R. Acceleration waves in solids. J Mech Phys Solids 1962;10(1):1–16 <http://www.sciencedirect.com/science/article/pii/0022509662900248>.
[29] Ida Y. Cohesive force across the tip of a longitudinal-shear crack and Griffith's specific surface energy. J Geophys Res 1972;77(20):3796–805. http://dx.doi.org/10.1029/JB077i020p03796.
[30] Kohler R, Hofstetter G. A cap model for partially saturated soils. Int J Numer Anal Meth Geomech 2008;32(8):981–1004 <http://doi.wiley.com/10.1002/nag.658>.
[31] Lou Y, Yoon JW, Huh H. Modeling of shear ductile fracture considering a changeable cut-off value for stress triaxiality. Int J Plast 2014;54:56–80 <http://www.sciencedirect.com/science/article/pii/S0749641913001617>.
[32] Lu G, Fall M. A coupled chemo-viscoplastic cap model for simulating the behavior of hydrating cemented tailings backfill under blast loading. Int J Numer Anal Methods Geomech 2015. http://dx.doi.org/10.1002/nag.2475. [in press].
[33] McDowell DL. Viscoplasticity of heterogeneous metallic materials. Mater Sci Eng: R: Rep 2008;62(3):67–123 <http://www.sciencedirect.com/science/article/pii/S0927796X08000430>.
[34] Motamedi M, Weed D, Foster C. Numerical simulation of mixed mode (i and ii) fracture behavior of pre-cracked rock using the strong discontinuity approach. Int J Solids Struct 2016:44–56 <http://www.sciencedirect.com/science/article/pii/S0020768316000494>.
[35] Motamedi MH, Foster CD. An improved implicit numerical integration of a non-associated, three-invariant cap plasticity model with mixed isotropic-kinematic hardening for geomaterials. Int J Numer Anal Meth Geomech 2015;39(17):1853–83. http://dx.doi.org/10.1002/nag.2372. nAG-14-0228.R1.
[36] Oliver J, Huespe A, Blanco S, Linero D. Stability and robustness issues in numerical modeling of material failure with the strong discontinuity approach. Comput Methods Appl Mech Eng 2006;195(52):7093–114. [computational Modelling of Concrete]. <http://www.sciencedirect.com/science/article/pii/S0045782505003920>.
[37] Ortiz M, Leroy Y, Needleman A. A finite element method for localized failure analysis. Comput Methods Appl Mech Eng 1987;61(2):189–214 <http://www.sciencedirect.com/science/article/pii/0045782587900041>.
[38] Ortiz M, Pandolfi A. Finite-deformation irreversible cohesive elements for three-dimensional crack-propagation analysis. Int J Numer Meth Eng 1999;44(9):1267–82. http://dx.doi.org/10.1002/(SICI)1097-0207(19990330)44:9<1267::AID-NME486>3.0.CO;2-7.
[39] Parvaneh S, Foster C. On numerical aspects of different updating schedules for tracking fracture path in strain localization modeling. Eng Fract Mech 2016;152:26–57 <http://www.sciencedirect.com/science/article/pii/S0013794415006621>.
[40] Qi M, Shao J, Giraud A, Zhu Q, Colliat J. Damage and plastic friction in initially anisotropic quasi brittle materials. Int J Plast 2016;82:260–82 <http://www.sciencedirect.com/science/article/pii/S0749641916300389>.
[41] Reddy BV, Kumar PP. Embodied energy in cement stabilised rammed earth walls. Energy Build 2010;42(3):380–5 <http://www.sciencedirect.com/science/article/pii/S0378778809002436>.
[42] Regueiro RA, Borja RI. Plane strain finite element analysis of pressure sensitive plasticity with strong discontinuity. Int J Solids Struct 2001;38(21):3647–72 <http://www.sciencedirect.com/science/article/pii/S002076830000250X>.
[43] Regueiro RA, Foster CD. Bifurcation analysis for a rate-sensitive, non-associative, three-invariant, isotropic/kinematic hardening cap plasticity model for geomaterials: Part I. Small strain. Int J Numer Anal Meth Geomech 2011;35(2):201–25 <http://doi.wiley.com/10.1002/nag.907>.
[44] Remmers JJ, de Borst R, Needleman A. The simulation of dynamic crack propagation using the cohesive segments method. J Mech Phys Solids 2013;56(1):70–92 <http://www.sciencedirect.com/science/article/pii/S0022509607001706>.
[45] Rinehart AJ, Bishop JE, Dewers T. Fracture propagation in Indiana limestone interpreted via linear softening cohesive fracture model. J Geophys Res: Solid Earth 2015;120(4):2292–308. http://dx.doi.org/10.1002/2014JB011624. 2014JB011624.
[46] Rudnicki J, Rice J. Conditions for the localization of deformation in pressure-sensitive dilatant materials. J Mech Phys Solids 1975;23(6):371–94. <http://www.sciencedirect.com/science/article/pii/0022509675900010>.
[47] Sancho JM, Planas J, Galves JC, Reyes E, Cendon DA. An embedded cohesive crack model for finite element analysis of mixed mode fracture of concrete*. Fatigue Fract Eng Mater Struct 2006;29(12):1056–65. http://dx.doi.org/10.1111/j.1460-2695.2006.01076.x.
[48] Scheider I, Brocks W. Simulation of cupcone fracture using the cohesive model. Eng Fract Mech 2003;70(14):1943–61. [cohesive Models]. <http://www.sciencedirect.com/science/article/pii/S0013794403001334>.
[49] Schroeder H. Sustainable building with earth. Springer; 2016.
[50] Silva R, Oliveira D, Schueremans L, Miranda T, Machado J. Effectiveness of the repair of unstabilised rammed earth with injection of mud grouts. Constr Build Mater 2016;127:861–87 <http://www.sciencedirect.com/science/article/pii/S0950061816316798>.
[51] Simo JC, Oliver J, Armero F. An analysis of strong discontinuities induced by strain-softening in rate-independent inelastic solids. Comput Mech 1993;12(5):277–96.
[52] Sorensen JD, Christensen HH. Danish requirements for robustness of structures: background and implementation. Struct Eng Int 2006;16(2):172–7.

[53] Spiezia N, Salomoni VA, Majorana CE. Plasticity and strain localization around a horizontal wellbore drilled through a porous rock formation. Int J Plast 2016;78:114–44 <http://www.sciencedirect.com/science/article/pii/S0749641915001886>.
[54] Starossek U, Haberland M. Measures of structural robustness requirements and applications. Proceedings of the 2008 structures congress - structures congress 2008: crossing the borders, vol. 314. ASCE; 2008. p. 1–10.
[55] Sun W, Chen Q, Ostien JT. Modeling the hydro-mechanical responses of strip and circular punch loadings on water-saturated collapsible geomaterials. Acta Geotech 2013. < http://link.springer.com/10.1007/s11440-013-0276-x > .
[56] Tennant AG, Foster CD, Venkatarama Reddy BV. Verification of masonry building code to flexural behavior of cement-stabilized soil block. J Mater Civ Eng 2013;25(3):303–7.
[57] Tjioe M, Borja RI. Pore-scale modeling of deformation and shear band bifurcation in porous crystalline rocks. Int J Numer Methods Eng 2016. http://dx.doi.org/10.1002/nme.5208. n/a–n/a Nme.5208.
[58] Tonge AL, Ramesh K. Multi-scale defect interactions in high-rate brittle material failure. Part i: Model formulation and application to {ALON}. J Mech Phys Solids 2016;86:117–49 <http://www.sciencedirect.com/science/article/pii/S0022509615302003>.
[59] Vorobiev O. Generic strength model for dry jointed rock masses. Int J Plast 2008;24(12):2221–47.
[60] Weed DA, Foster CD, Motamedi MH. A robust numerical framework for simulating localized failure and fracture propagation in frictional materials. Acta Geotech 2017;12(2):253–75. http://dx.doi.org/10.1007/s11440-016-0474-4.
[61] Wong T, Baud P. The brittle-ductile transition in porous rock: a review. J Struct Geol 2012;44(0):25–53 <http://www.sciencedirect.com/science/article/pii/S0191814112001708>.
[62] Xie S, Shao J. Elastoplastic deformation of a porous rock and water interaction. Int J Plast 2006;22(12):2195–225 <http://www.sciencedirect.com/science/article/pii/S0749641906000374>.
[63] Xie SY, Shao JF. Experimental investigation and poroplastic modelling of saturated porous geomaterials. Int J Plast 2012;39:27–45.
[64] Zami MS, Lee A. Economic benefits of contemporary earth construction in low-cost urban housing – state-of-the-art review. J Build Appraisal 2010;5(3):259–71. http://dx.doi.org/10.1057/jba.2009.32.